Measurement of the helium 2^3S metastable atom density by observation of the change in the 2^3S-2^3P emission line shape due to radiation reabsorption

T Shikama[a)], S Ogane[a)], Y Iida[b)], and M Hasuo[a)]

[a)]Department of Mechanical Engineering and Science,
Graduate School of Engineering, Kyoto University, Kyoto 615-8540, Japan
[b)]Bunkokeiki Co., Ltd., Hachioji, Tokyo 192-0033, Japan

Abstract

In helium discharge plasmas, the relative emission intensities of the fine-structure transitions belonging to the HeI 2^3S-2^3P transition can be affected by radiation reabsorption. Since the magnitude of the reabsorption depends on the density and temperature of the 2^3S metastable atoms, their density can be determined by measuring the 2^3S-2^3P emission line shape using a high wavelength-resolution spectrometer. In this study, the applicable conditions of the method in terms of the opacity and line broadening are revealed, and possible causes of errors in the measurement, *i.e.,* spatial distributions of the density and temperature and the effects of external magnetic and electric fields, are investigated. The effect of reabsorption under an external magnetic field is experimentally confirmed using a glow discharge plasma installed in a superconducting magnet.

I Introduction

Helium 2^1S and 2^3S metastable atoms play key roles in discharge plasmas because of their relatively long radiative lifetimes of $\sim 2 \times 10^{-2}$ [1] and 8×10^3 s [2] and large excitation energies of 20.6 and 19.8 eV [2], respectively. In the sustainment and control of discharge plasmas, they are known to affect the plasma parameters through the Penning ionization and secondary electron emission under both low-pressure [3–6] and atmospheric-pressure [7–11] conditions. Their importance has also been recognized in their applications to atom lithography [12, 13], ambient desorption ionization [14], and the removal of hydrocarbon contamination in EUV lithography apparatus [15], in which the local deposition of the excitation energy on the surface is utilized. Moreover, their densities are essential for some types of plasma diagnostics, such as collisional-radiative (CR) model analysis in terms of the validity of the quasi-steady-state (QSS) approximation [16–19] and measurements of the reduced electric field in an electric double layer [20] and alpha particles in fusion-related plasmas [21].

To clarify the roles that the metastable atoms play in these plasmas and to control the related engineering processes, it is necessary to evaluate their densities. As a diagnostic method for the 2^3S atom density, self-absorption spectroscopy was adopted for a long time [22–25]. In this method, emission emanating from a plasma is reflected back into the plasma and the consequent absorption is observed. Once lasers became readily available, laser-induced fluorescence spectroscopy and tunable diode laser absorption spectroscopy (TDLAS) became the standard diagnostics, and these methods have been successfully implemented in both low-pressure [3, 5, 21, 26] and atmospheric-pressure discharge plasmas [8–11, 27, 28].

We present an alternative method using optical emission spectroscopy, in which the spectral line shape of the 2^3S-2^3P transition, in particular, the variation of the relative emission intensities among the fine-structure transitions caused by radiation reabsorption, is measured. This transition is known to be sensitive to radiation reabsorption because of the relatively large absorption oscillator strength and larger density in the 2^3S state than in the other excited states. Compared with the laser-based methods, this method has the advantages of a compact experimental setup and applicability to plasmas in which the transmission measurement of laser light is difficult, for instance, those formed in commercial devices or in the divertor region of fusion-related plasmas. To the best of our knowledge, the method was originally proposed by Daviaud *et al.* [29], who evaluated the 2^3S atom density in a surface wave discharge plasma. We have recently developed a high wavelength-resolution spectrometer optimized for the observation of the 2^3S-2^3P transition spectral line shape [30], and we applied the method to two types of glow discharge plasmas with different spatial distributions of the 2^3S atom density [31]. In the present paper, we reveal the applicable conditions of the method in detail and also investigate the effects of external magnetic and electric fields. The latter is especially important to improve the accuracy of density estimation, since it can significantly affect radiation reabsorption through the wavelength splitting of the spectral line, variations in the emissivity and absorption, and the necessity of taking polarization into account.

II Methods

The HeI 2^3S-2^3P transition consists of three fine-structure transitions as listed in Table 1. A spectral line shape calculated in a case without absorption and with the Doppler broadening at a temperature of 1000 K is shown in the inset of Fig. 1; the vertical lines represent the wavelengths and relative emission intensities of the fine-structure transitions. They have a unique lower state and an identical spontaneous emission coefficient, while the magnitudes of their absorption oscillator strengths are proportional to the statistical weight of the upper state.

We analyze the radiation reabsorption of the HeI 2^3S-2^3P emission by using the radiative transfer equation for the individual fine-structure transitions. The equation is expressed by neglecting stimulated emission as

$$\frac{\mathrm{d}I_{qp}(s,\Delta\nu)}{\mathrm{d}s} = -\sum_{i,j}\kappa_{ij}(s,\Delta\nu)I_{qp}(s,\Delta\nu) + \epsilon_{qp}(s,\Delta\nu), \tag{1}$$

where $I_{qp}(s,\Delta\nu)$ is the emission intensity, p and q respectively represent the lower and upper J-levels with J the total angular momentum quantum number, s is the coordinate along the viewing chord, $\Delta\nu$ is the frequency shift from a given line center, $\kappa_{pq}(s,\Delta\nu)$ is the absorption coefficient, $\epsilon_{qp}(s,\Delta\nu)$ is the spectral emissivity, and the summation is taken over all the transitions. $\kappa_{pq}(s,\Delta\nu)$ and $\epsilon_{qp}(s,\Delta\nu)$ are defined as

$$\kappa_{pq}(s,\Delta\nu) = \frac{e^2}{4m_\mathrm{e}c\epsilon_0}n_p\alpha_p(s)f_{pq}P_{pq}(s,\Delta\nu), \tag{2}$$

$$\epsilon_{qp}(s,\Delta\nu) = \frac{h\nu_{qp}}{4\pi}n_q\alpha_q(s)A_{qp}P_{qp}(s,\Delta\nu), \tag{3}$$

where e is the elementary charge, m_e is the electron mass, c is the velocity of light, ϵ_0 is the vacuum permittivity, $n_{p(q)}$ is the population density at the plasma center, $\alpha_{p(q)}(s)$ is a function describing the spatial distribution of the population density, f_{pq} is the absorption oscillator strength, $P_{pq(qp)}(s,\Delta\nu)$ is the absorption (emission) line profile, ν_{qp} is the transition frequency, and A_{qp} is the spontaneous emission coefficient. For the emission and absorption, we assume complete frequency redistribution.

If we assume a one-dimensional plasma with length L, the emission intensity outside the plasma is readily obtained as

$$I_{qp}(\Delta\nu) = \int_0^L \epsilon_{qp}(s, \Delta\nu) \exp\left[-\int_s^L \sum_{i,j} \kappa_{ij}(s', \Delta\nu) \mathrm{d}s' \right] \mathrm{d}s. \tag{4}$$

In particular, when the plasma is homogeneous, $I_{qp}(\Delta\nu)$ can be written as

$$I_{qp}(\Delta\nu) = \frac{\epsilon_{qp}(\Delta\nu)}{\sum_{i,j} \kappa_{ij}(\Delta\nu)} \left\{ 1 - \exp\left[-\sum_{i,j} \kappa_{ij}(\Delta\nu) L \right] \right\}. \tag{5}$$

The solid line in Fig. 1 shows the calculated ratio of the emission intensities $\int [I_{21}(\Delta\nu) + I_{11}(\Delta\nu)]\mathrm{d}(\Delta\nu) / \int I_{01}(\Delta\nu)\mathrm{d}(\Delta\nu)$ in a homogeneous plasma when $P_{pq}(s, \Delta\nu)$ and $P_{qp}(s, \Delta\nu)$ undergo the Doppler broadening at a temperature of 1000 K. We henceforth denote the spatial distributions of the upper and lower state densities under this condition, *i.e.*, $\alpha_p(s) = \alpha_q(s) = 1$, as case (i). The abscissa of the figure is a variable, which is a measure of the opacity for the $2^3\mathrm{S}_1$–$2^3\mathrm{P}_0$ transition and is defined using the subscripts p and q as

$$\tau_{pq} = \kappa_{pq}(s_0, \Delta\nu = 0)L = \frac{e^2}{4 m_\mathrm{e} \epsilon_0} \sqrt{\frac{M}{2\pi k_\mathrm{B} T_p(s_0)}} \frac{f_{pq}}{\nu_{qp}} n_p L, \tag{6}$$

where s_0 denotes the position at the plasma center, M is the atomic mass, k_B is Boltzmann's constant, and T_p is the lower state temperature. Note that τ_{pq} is equivalent to the optical depth only when $\alpha_p(s)$ and $T_p(s)$ are constants. In Eq. (6), f_{12} and f_{11} are related to f_{10} as $f_{12} = 5f_{10}$ and $f_{11} = 3f_{10}$, so that if we neglect slight differences in ν_{qp}, the equations $\tau_{12} = 5\tau_{10}$ and $\tau_{11} = 3\tau_{10}$ hold. In the optically thin case ($\tau_{10} \ll 1$), the emission intensity ratio approaches $\int [\epsilon_{21}(\Delta\nu) + \epsilon_{11}(\Delta\nu)]\mathrm{d}(\Delta\nu) / \int \epsilon_{01}(\Delta\nu)\mathrm{d}(\Delta\nu)$, which becomes 8 when the upper and lower state population densities follow the statistical weight. On the other hand, in the optically thick case ($\tau_{10} \gg 1$), the ratio approaches $\int [S_{21}(\Delta\nu) + S_{11}(\Delta\nu)]\mathrm{d}(\Delta\nu) / \int S_{01}(\Delta\nu)\mathrm{d}(\Delta\nu)$, where we define the source function as $S_{qp}(\Delta\nu) = \epsilon_{qp}(\Delta\nu) / \sum_{i,j} \kappa_{ij}(\Delta\nu)$. In the intermediate opacity case, the intensity ratio decreases with increasing τ_{10}, and utilizing this dependence, we can in principle determine n_0, the $2^3\mathrm{S}$ atom density. Under the above assumptions, the intermediate opacity range is approximately $10^{-2} < \tau_{10} < 10$, which is equivalent to a $2^3\mathrm{S}$ atom density of about 10^{16}–10^{19} m^{-3} when $L = 10$ mm.

The following two conditions are required for the application of this method: (i) the absorption is in the intermediate opacity range and (ii) the spectral line broadening is sufficiently small to observe the relative intensities among the fine-structure transitions. For the first requirement, the range of the previously reported $2^3\mathrm{S}$ atom densities in various low- and atmospheric-pressure discharge plasmas considerably overlap with that of the above-mentioned detectable density. The second requirement imposes limitations on the electron density and helium atom temperature and pressure through the Stark, Doppler, and pressure broadening, respectively. The Stark broadening coefficient has been calculated to be 1.56×10^{-21} pm/m^{-3} for an electron temperature of 4×10^4 K [32, 33], where the effect of ion impact is not taken into account, while the pressure broadening coefficient has been measured to be 5.44×10^{-4} pm/Pa for an atmospheric-pressure plasma by TDLAS [27]. If we consider either of the three types of broadening, broadening with a full width at half maximum (FWHM) of 120 pm, which is the difference between the wavelengths of the large and small peaks in the inset of Fig. 1, corresponds to an electron density of 7.7×10^{22} m^{-3}, a helium atom temperature of 8.3 eV, and a helium atom pressure of 220 kPa. The coexistence of these different types of broadening in the actual plasma restricts these numbers to smaller values.

A Effects of spatial distributions

Since the emission intensity ratio depends on the spatial distributions of $\alpha_{p(q)}(s)$ and $P_{pq(qp)}(s)$, appropriate assumptions for these functions will be crucial for the accurate measurement of the 2^3S atom density. Here we evaluate possible errors in the estimated τ_{10} caused by variations in the spatial distributions of $\alpha_{p(q)}(s)$ and $P_{pq(qp)}(s)$ when the emission and absorption line profiles are identical and have only the Doppler broadening.

The ratios are calculated in two additional cases with a spatially uniform temperature of 1000 K: (ii) $\alpha_p(s) = \alpha_q(s) = J_0(j_{01}|s - L/2|/(L/2))$, (iii) $\alpha_p(s) = 1$ and $\alpha_q(s) = J_0(j_{01}|s - L/2|/(L/2))$, where J_0 and $j_{01} \simeq 2.405$ denote the zeroth-order Bessel function and its first zero point, respectively. The calculated ratios are shown in Fig. 1 as dashed and dot-dashed lines. In case (ii), the absorption of the emission is smaller than that in case (i), and the curve is scalable to that in case (i) by dividing τ_{10} by 1.6. On the other hand, in case (iii), the contribution of the emission from the edge region (near $s = 0$ and L), which has relatively small absorption, is less significant than in case (i); thus, the absorption appears to increase. The curve is approximately scalable to that in case (i) by multiplying τ_{10} by 1.4 when $\tau_{10} \leq \sim 1$, but the deviation becomes significantly larger for larger τ_{10}.

In these calculations, $\alpha_{p(q)}(s)$ represented by unity and the Bessel function correspond to conditions in which the mean free path of the excited atoms is on the same order or larger than L and is sufficiently smaller than L, respectively. The actual $\alpha_{p(q)}(s)$ is among the above-mentioned three cases, but the error in τ_{10} due to an inappropriate assumption for $\alpha_{p(q)}(s)$ is less than about a factor of 2 when $\tau_{10} \leq \sim 1$.

In the application of this method, we can deduce the atomic temperature from the observed Doppler broadening in the spectral line shape. The nonuniform spatial distribution of the temperature will, however, increase the error in τ_{10} estimated under the assumption of a uniform temperature. To evaluate possible errors, we calculated the intensity ratio assuming a quadratic temperature distribution:

$$T(s) = 1000 - 700[(s - L/2)/(L/2)]^2. \tag{7}$$

For all three cases, the variations in the estimated τ_{10} are less than 10% from the uniform-temperature cases when the intensity ratio is within 2−7.

B Effects of external magnetic and electric fields

Under static external magnetic and electric fields, the emission and absorption are affected by the Zeeman and Stark effects. Since these effects can change the spectral line shape and thereby the magnitude of the absorption, we investigate in detail their contributions to radiation reabsorption. We calculate the effects by using a perturbation theory for degenerate levels [34]. The effects are approximately treated as first-order perturbations to the unperturbed energy levels taken from a database [2]. In addition to the perturbed energy levels, the magnitude of the square of the transition matrix element $\mathfrak{S}_{qp} = \sum_i |\langle \Psi_q | r_i | \Psi_p \rangle|^2$ is evaluated, where $\Psi_{p(q)}$ represents the wavefunction resolved into the magnetic sublevels, r_i is the spherical tensor component of the electric dipole moment, and we redefine p and q to denote the lower and upper levels divided into the magnetic sublevels, respectively. The line strength without the external fields, which is required to determine the absolute value of $\mathfrak{S}_{qp}$, is taken from a database [2]. The spontaneous emission coefficient and absorption oscillator strength are defined [35] as

$$A_{qp} = \frac{16\pi^3 \nu_{qp}^3 e^2}{3\epsilon_0 h c^3} \mathfrak{S}_{qp}, \tag{8}$$

$$f_{pq} = \frac{8\pi^2 m_e \nu_{qp}}{3h} \mathfrak{S}_{qp}. \tag{9}$$

We first consider the effect of a magnetic field, and for simplicity assume that the observation direction is perpendicular to the field direction. Then the lights emitted or absorbed through the π ($\Delta M = 0$) and σ ($\Delta M = \pm 1$) transitions are mutually orthogonal and linearly polarized, where ΔM is the variation of the magnetic quantum number, and thus the π and σ transitions do not absorb light associated with mutual transitions. Under these conditions, the radiative transfer equation (1) can be written for the π and σ transitions as

$$\frac{\mathrm{d}I_{qp}(s,\Delta\nu)}{\mathrm{d}s} = C_{qp}\left[-\sum_{i,j}\kappa_{ij}(s,\Delta\nu)I_{qp}(s,\Delta\nu) + \epsilon_{qp}(s,\Delta\nu)\right] \quad \text{with} \quad C_{qp} = \begin{cases} 1 & (\pi) \\ \frac{1}{2} & (\sigma) \end{cases}, \tag{10}$$

where the summation is taken over all π or σ transitions. The calculation can be extended to the case with an arbitrary field direction by using the vector radiative transfer equation [36,37]. The present case corresponds to $\gamma = \pi/2$ and $\chi = 0$, where γ and χ are the angles giving the direction of the magnetic field defined in Fig. 1 of Ref. [36].

In the calculation, we assume a one-dimensional homogeneous plasma in which the atomic temperature is 1000 K. Figure 2(a) shows the calculated spectral line shapes with and without absorption at field strengths of 0, 0.3, 0.8, and 3 T, where the ordinate shows the relative emission intensity. Note that the continuous variation of the transition wavelengths and their relative intensities without absorption are shown in Fig. 3(a), and the numerical values of the wavelength and $\mathfrak{S}_{qp}$ are tabulated in Tabs. A1 and A2. Figure 2(b) shows the calculated variation of the total emission intensity $I = \int \sum_{p,q} I_{qp}(\Delta\nu)\mathrm{d}(\Delta\nu)$ with the magnetic field strength when $\tau_{10} = 0.5$; in the figure, the total intensity without the absorption is normalized to unity. On applying an external magnetic field, the splitting of the transition wavelength reduces the superposition of the absorption line profiles, and thus the magnitude of the absorption as can be seen in the change in the spectral line shape from (i) to (ii) in Fig. 2(a). Then, when the field strength is increased to about 0.6−1.0 T, the σ-components belonging to the $2^3\mathrm{S}_1$−$2^3\mathrm{P}_0$ and $2^3\mathrm{S}_1$−$2^3\mathrm{P}_{1,2}$ transitions become superposed as can be seen in (iii), and the absorption locally increases. With a further increase in the field strength, the Zeeman effect reaches the so-called Paschen-Back limit, and the superposition of the absorption line profiles gradually increases; see also Fig. 3(a). The spectral line shape in this phase is shown in (iv) in Fig. 2(a). From these calculation results, we can see that the presence of the magnetic field reduces the absorption to about 60%, although the extent of the reduction depends on the emission and absorption line profiles as well as the field strength.

Under the external magnetic field, the two peaks in the spectrum, which were used for the analysis in the previous subsection, are no longer observable. We therefore evaluate τ_{10} on the basis of the relative intensities of all the transitions among the magnetic sublevels, namely, by considering the deformation of the entire spectral line shape by the absorption. To confirm the applicability of this procedure, the derivative $|(1/I_0)\mathrm{d}I/\mathrm{d}(\log_{10}\tau_{10})|$ is calculated as a measure of the deformation, where I_0 is the total emission intensity without the absorption. It can be seen from the calculation results shown in Fig. 4 that even under an external magnetic field, the magnitude of the deformation is similar to that in the case without the field. The applicable opacity range in terms of the $2^3\mathrm{S}$ atom density becomes about 1.7 times larger than that in the cases of 0.3 and 3 T owing to the decrease in the absorption.

Compared with the magnetic field effect, the electric field effect is significantly smaller. Figure 3(b) shows the wavelength shifts plotted against the field strength. When the field strength is smaller than 1×10^7 V/m, which is an upper limit for typical discharge plasmas [38–40], the wavelength splitting is smaller than 2 pm, which is much smaller than the Doppler broadening. We can therefore neglect the electric field effect.

III Experiments

To confirm the effect of a magnetic field on radiation reabsorption, we carried out experiments using a dc glow discharge plasma under a uniform external magnetic field. A schematic diagram of the apparatus is shown in Fig. 5. A cylindrical discharge tube made of glass with an inner diameter of 5 mm and a length of 190 mm was adopted, and the tube was inserted in the bore of a cryogen-free superconducting magnet (Cryogenic 1721) with its axis aligned along the field direction. The inhomogeneity of the field strength is less than 0.25% over a 10-mm-diameter sphere at the center of the tube. The inside of the discharge tube was filled with pure helium with a pressure of 501 Pa and the discharge current was set to 3 mA.

The emission from the discharge tube was collected by a quartz optical fiber (Mitsubishi Cable Industries ST50A-FV; core diameter 50 μm, cladding diameter 125 μm, NA 0.2) directed perpendicular to the discharge tube axis. The end surface of the optical fiber was located at the center of the tube and was separated by 20 mm from the axis. The whole cross section of the tube was observed simultaneously through the acceptance angle of the optical fiber, which is about 11.5°, and the diameter of the viewing area on the axis was about 8 mm. The light transferred via the optical fiber was dispersed by a near-infrared interference spectrometer [30], which consists of a tunable Fabry-Perot etalon. We obtained a spectrum by scanning the cavity length of the etalon using a piezoelectric element. To improve the S/N ratio, 500 spectra were averaged, and data points within an interval of about 2.7 pm were reduced to their average value. The instrumental function measured using a single-mode diode-laser light was represented by a Lorentzian function with an FWHM of 17.5 pm. The markers in Figs. 6(a)-(c) show the measured spectral line shapes under magnetic field strengths of 0, 247, and 497 mT, respectively. Under the present experimental conditions, the spectral line broadening is dominated by the Doppler broadening and the instrumental function, and the pressure broadening and the Stark broadening are negligible [31].

A Radiative transfer in the cross section of a cylindrical plasma

Figure 7 shows a schematic diagram of the cross section of a cylindrical plasma with radius R. We define the $\{xyz\}$ coordinate system as shown in the figure, where a uniform magnetic field is applied in the z-direction; we assume that the plasma is axially symmetric and uniform in the axial direction. We approximate that the observed line-integrated emission intensity per unit axial length is expressed as

$$I_{qp}(\Delta\nu) = 2\int_0^R \int_{-x_j}^{x_j} C_{qp}\epsilon_{qp}(\rho,\Delta\nu)\exp\left[-\int_x^{x_j}\sum_{i,j} C_{ji}\kappa_{ij}(\rho',\Delta\nu)\mathrm{d}x'\right]\mathrm{d}x\mathrm{d}y, \qquad (11)$$

where x_j, ρ, and ρ' are given as $x_j = \sqrt{R^2 - y^2}$, $\rho = \sqrt{x^2 + y^2}$, and $\rho' = \sqrt{x'^2 + y^2}$, and we represent the emission and absorption line profiles by an identical Gaussian function corresponding to the Doppler broadening with a spatially uniform temperature. Since the adopted optical fiber has a finite acceptance angle, a part of the view is not parallel to the xy-plane. For that part of the view, the observed light travels longer distance in the plasma. In addition, the relative emission intensities between the π and σ components changes and the π and σ transitions absorb light associated with mutual transition. The elongation of the light traveling distance is, however, smaller than $1/\cos(11.5°) \simeq 2\%$, and the changes in the emission intensities between the π and σ components is smaller than $\sin^2(11.5°) \simeq 4\%$. We therefore neglected the effect of the oblique observation.

In the calculation using Eq. (11), we determined the temperature from the observed Doppler broadening, and regarded R as the inner radius of the discharge tube since the plasma is extin-

guished on the surface. We assumed that the electron temperature is spatially uniform, while the spatial distribution of the electron density is represented by the zeroth-order Bessel function, so that the spatial distributions of the upper and lower state helium atom densities are expressed as $\alpha_p(\rho) = \alpha_q(\rho) = J_0(j_{01}\rho/R)$. This assumption is based on the fact that the mean free path of the elastic collision between the atoms is less than 0.2 mm and sufficiently smaller than R, where we assume that the collision de-excites the 2^3S and 2^3P atoms.

We fitted the calculated spectral line shapes to the measured ones with the intensity, temperature, and 2^3S atom density on the axis of the plasma as adjustable parameters. Note that the 2^3P atom density on the axis does not affect the relative intensities among I_{qp}. Since the broadening of the measured spectral lines is dominated by the instrumental function, we further approximate the relative intensities of the transitions among the magnetic sublevels using $\int I_{qp}(\Delta\nu)\mathrm{d}(\Delta\nu)$, and each transition has a broadening that is a convolution of the Doppler broadening and the instrumental function. This approximation will slightly overestimate the temperature. The fitting curves are shown in Fig. 6 as the solid lines. The determined temperatures and τ_{10} are given in the figures, where τ_{10} is defined by Eq. (6) but with L replaced by R. The fitting curves closely reproduce the measurements, and the relative intensities of the transitions among the magnetic sublevels are significantly changed from their statistical weights owing to radiation reabsorption. The 2^3S atom densities on the plasma axis are estimated to be 8.0, 5.3, and 3.0 $\times$ 10^{18} m^{-3} for Figs. 6(a)−(c), respectively, and the order of the densities is comparable to that obtained for discharge plasmas produced under similar experimental conditions [23–25]. The validity of the obtained τ_{10} was qualitatively confirmed by observing the increase in τ_{10} with the discharge current [31].

In the present results, a decrease in τ_{10} with increasing field strength was observed. Possible causes of this tendency are a decrease in the 2^3S atom density and changes in the radial distributions of the 2^3S and 2^3P atom densities from the Bessel function to a more peaky distribution on applying a magnetic field. Regarding the first cause, it might be due to a decrease in the electron density by anomalous cross-field diffusion [41]. We have not measured the electron density, but that is expected to be smaller than 10^{17} m^{-3} on the basis of experimental results using a similar glow discharge tube [42, 43]. Meanwhile, the electron temperature in glow discharge plasmas is typically smaller than 10 eV [16, 44]. In a glow discharge plasma with these parameters, the 2^3S and 2^3P atom densities are nearly proportional to the electron density as reported in Fig. 12 of Ref. [16]. In the present study, the change of the 2^3P atom density can be obtained from the emission intensities evaluated from the fitted spectral line shapes extrapolated to the case without absorption. In Figs. 6(a)−(c), the ratio of the intensities is about 1.0:0.51:0.23, respectively. The ratio is close to that of τ_{10} but rather smaller, which can be explained by a weaker dependence of the 2^3S atom density on the electron density than the 2^3P atom density. Note that the helium pressure of the present experiment is about 10 times larger than that of the reference, but this may not affect the above discussion since the pressure is fixed for all the conditions. The effect of the second cause can be determined by performing spatially resolved measurement, which is a task for a future study.

IV Conclusions

We presented a passive emission spectroscopic method for measuring the helium 2^3S metastable atom density by observing the 2^3S−2^3P emission line shape. The method is applicable when the opacity of the $2^3\mathrm{S}_1$−$2^3\mathrm{P}_0$ fine-structure transition is intermediate and the spectral line broadening is sufficiently small to resolve the fine-structure transitions. The former corresponds to a 2^3S atom density of approximately 10^{16} to 10^{19} m^{-3} with an absorption length of 10 mm, while the latter requires the upper bounds of the electron density, helium atom temperature,

and helium atom pressure to be 7.7×10^{22} m^{-3}, 8.3 eV, and 220 kPa, respectively.

Possible errors expected in applications to actual discharge plasmas were calculated. The spatial distributions of the upper and lower state densities and the temperature result in errors in the estimated τ_{10} of about 200% and 10%, respectively. The former number is, however, in the worst case, and it can be smaller by an appropriate assumption of the distributions. The presence of an external magnetic field reduces the absorption to about 60% when the magnetic field strength is larger than about 0.5 T because of decrease in the superposition of the absorption line profiles.

We applied the method to a cylindrical glow discharge plasma under various external magnetic fields and confirmed that the measured spectral line shapes are closely reproduced by the calculation and that we can determine the 2^3S atom densities.

Acknowledgments

This work was supported in part by a Kurata Grant from Kurata Memorial Hitachi Science and Technology Foundation and a NIFS collaborative research program (NIFS14KUTR099). One of the authors (TS) thanks Prof. M. Goto at the National Institute for Fusion Science for the discussion about the calculation of the Stark effect.

References

[1] Van Dyck Jr. R S, Johnson C E, and Shugart H A 1971 *Phys. Rev. A* **4**, 1327.

[2] NIST Atomic Spectra Database.

[3] Benedictis S D and Dilecce G 1995 *J Phys. D: Appl. Phys.* **28**, 2067.

[4] Katsch H-M, Quandt E, and Schneider Th 1996 *Plasma Phys. Controlled Fusion* **38**, 183.

[5] Millard M W, Yaney P P, Ganguly B N, and DeJoseph Jr. C A 1998 *Plasma Sources Sci. Technol.* **7**, 389.

[6] Baguer N, Bogaerts A, and Gijbels R 2003 *J. Appl. Phys.* **93**, 47.

[7] Li Q, Zhu X, Li F, and Pu Y 2010 *J. Appl. Phys.* **107**, 043304.

[8] Niemi K, Waskoenig J, Sadeghi N, Gans T, and O'Connell D 2011 *Plasma Sources. Sci. Technol.* **20**, 055005.

[9] Niermann B, Hemke T, Babaeva N Y, Böke M, Kushner M J, Mussenbrock T, and Winter J 2011 *J. Phys. D: Appl. Phys.* **44**, 485204.

[10] Cardoso R P, Belmonte T, Henrion G, and Sadeghi N 2006 *J. Phys. D: Appl. Phys.* **39**, 4178.

[11] Winter J, Santos Sousa J, Sadeghi N, Schmidt-Bleker A, Reuter S, and Puech V 2015 *Plasma Sources Sci. Technol.* **24**, 025015.

[12] Nowak S, Pfau T, and Mlynek J 1996 *Appl. Phys. B* **63**, 203.

[13] Allred C S, Reeves J, Corder C, and Metcalf H 2010 *J. Appl. Phys.* **107**, 033116.

[14] Cody R B, Laramée J A, and Durst H D 2005 *Anal. Chem.* **77**, 2297.

[15] Lytle W M, Andruczyk D, and Ruzic D N 2013 *J. Vac. Sci. Technol. B* **31**, 011603.

[16] Fujimoto T 1979 *J. Quant. Spectrosc. Radiat. Transfer* **21**, 439.

[17] Goto M 2003 *J. Quant. Spectrosc. Radiat. Transfer* **76**, 331.

[18] Iida Y, Kado S, and Tanaka S, 2010 *Phys. Plasmas* **17**, 123301.

[19] Sawada K, Goto M, and Ezumi N 2011 *Plasma Fusion Res.* **6**, 1401010.

[20] Williamson J M and Ganguly B N 2001 *Phys. Rev. E* **64**, 036403.

[21] Okamoto A, Shinto K, Kitajima S, and Sasao M 2007 *Plasma Fusion Res.* **2**, S1044.

[22] Harrison J A 1959 *Proc. Phys. Soc.* **73**, 841.

[23] Browne P G and Dunn M H 1973 *J. Phys. B: At. Mol. Phys.* **6**, 1103.

[24] Ichikawa Y and Teii S 1980 *J. Phys. D: Appl. Phys.* **13**, 1243.

[25] Suh M H, Hong X, and Miller T A 1998 *Chem. Phys.* **228**, 145.

[26] Dinklage A, Lokajczyk T, and Kunze H J 1996 *J. Phys. B: At. Mol. Phys.* **29**, 1655.

[27] Tachibana K, Kishimoto Y, and Sakai O 2005 *J. Appl. Phys.* **97**, 123301.

[28] Urabe K, Morita T, Tachibana K, and Ganguly B N 2010 *J. Phys. D: Appl. Phys.* **43**, 095201.

[29] Daviaud S, Gousset G, Marec J, and Bloyet E 1990 *J. Phys. D* **23**, 856.

[30] Ogane S, Shikama T, Zushi H, and Hasuo M 2015 *Rev. Sci. Instrum.* **86**, 103507.

[31] Shikama T, Ogane S, Ishii H, Iida Y, and Hasuo M 2014 *Jpn. J. Appl. Phys.* **53**, 086101.

[32] Dimitrijević M S and Sahal-Bréchot S 1984 *J. Quant. Spectrosc. Radiat. Transfer* **31**, 301.

[33] Dimitrijević M S and Sahal-Bréchot S 1990 *Astron. Astrophys. Suppl. Ser.* **82**, 519.

[34] Goto M "Plasma Polarization Spectroscopy," ed. by Fujimoto T and Iwamae A 2007 *Springer*, Ch.2.

[35] Cowan R D "The Theory of Atomic Structure and Spectra" 1981 *University of California Press*, p.404.

[36] Jefferies J, Lites B W, and Skumanich A 1989 *Astrophys. J.* **343**, 920.

[37] Rees D E, Murphy G A, and Durrant C J 1989 *Astrophys. J.* **339**, 1093.

[38] Greenberg K E and Hebner G A 1993 *Appl. Phys. Lett.* **63**, 3282.

[39] Kuracia M M and Konjević N 1997 *Appl. Phys. Lett.* **70**, 1521.

[40] Sretenović G B, Krstić I B, Kovačević V V, Obradović B M, and Kuracia M M 2011 *Appl. Phys. Lett.* **99**, 161502.

[41] Chen F F "Introduction to Plasma Physics and Controlled Fusion, 2nd ed." 1974 *Plenum Press*, pp.174-175.

[42] Uetani Y and Fujimoto T 1984 *Opt. Commun.* **49**, 258.

[43] Uetani Y and Fujimoto T 1985 *Opt. Commun.* **55**, 457.

[44] Shikama T, Kado S, Kurihara K, and Kuwahara Y 2009 *Phys. Plasmas* **16**, 033504.

Table 1: Data of fine-structure transitions belonging to the HeI 2^3S-2^3P transition [2]. λ, A, and f represent the wavelength, spontaneous emission coefficient, and absorption oscillator strength, respectively.

transition	λ (nm)	A ($\times 10^7$ s^{-1})	f ($\times 10^{-1}$)
$2^3S_1-2^3P_0$	1082.9091140	1.0216	0.59902
$2^3S_1-2^3P_1$	1083.0250105	1.0216	1.7974
$2^3S_1-2^3P_2$	1083.0339773	1.0216	2.9958

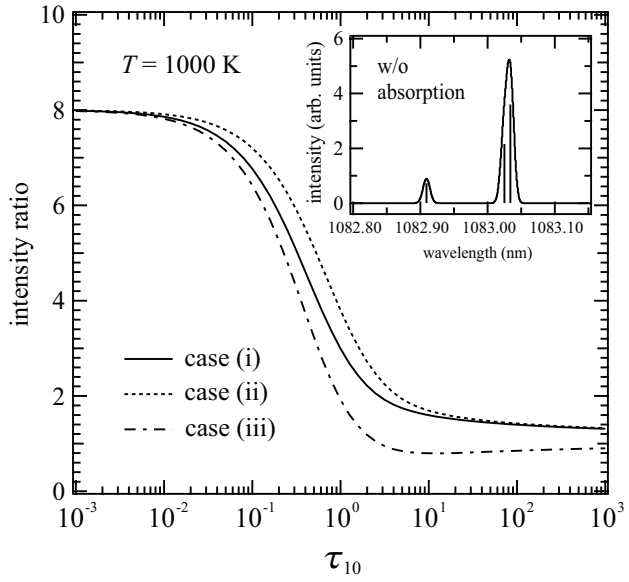

Figure 1: Calculated ratio of the emission intensities as a function of τ_{10}. The three cases are (i) $\alpha_p(s) = \alpha_q(s) = 1$, (ii) $\alpha_p(s) = \alpha_q(s) = J_0(j_0|s - L/2|/(L/2))$, and (iii) $\alpha_p(s) = 1$ and $\alpha_q(s) = J_0(j_0|s - L/2|/(L/2))$. The inset shows the spectral line shape without absorption and with the Doppler broadening at a temperature of 1000 K.

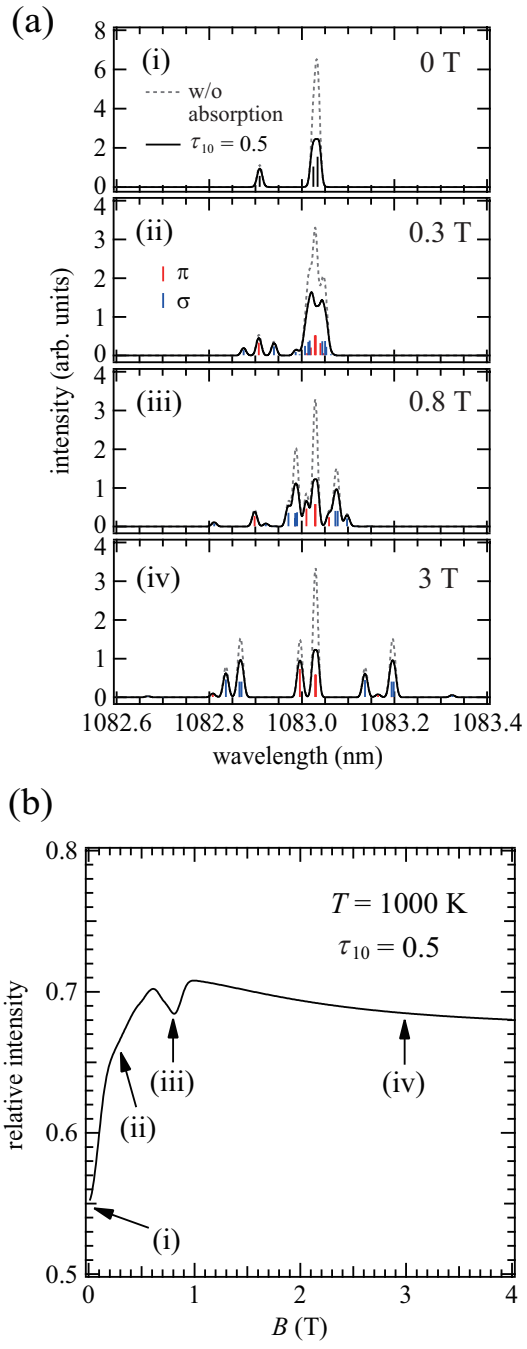

Figure 2: (a) Calculated spectral line shapes with and without absorption. (b) Variation of the total emission intensity as a function of the magnetic field strength.

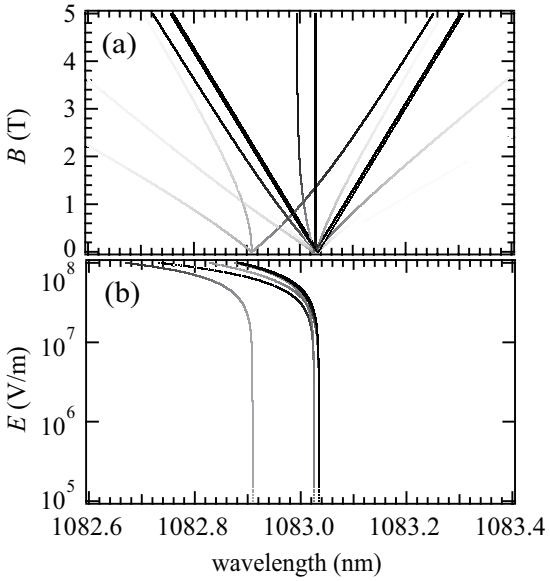

Figure 3: Variations in the wavelength with (a) magnetic and (b) electric fields. The relative emission intensity is indicated by gray-scale.

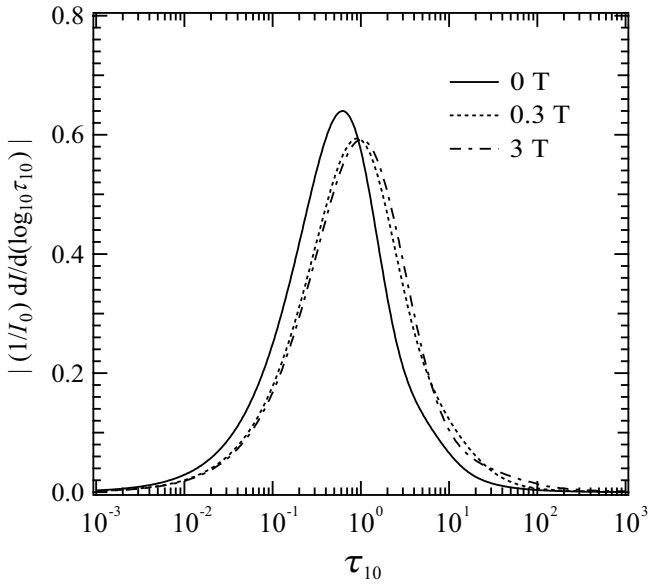

Figure 4: Calculated curves of $|(1/I_0)\mathrm{d}I/\mathrm{d}(\log_{10}\tau_{10})|$ as a measure of deformation of the entire spectral line shape.

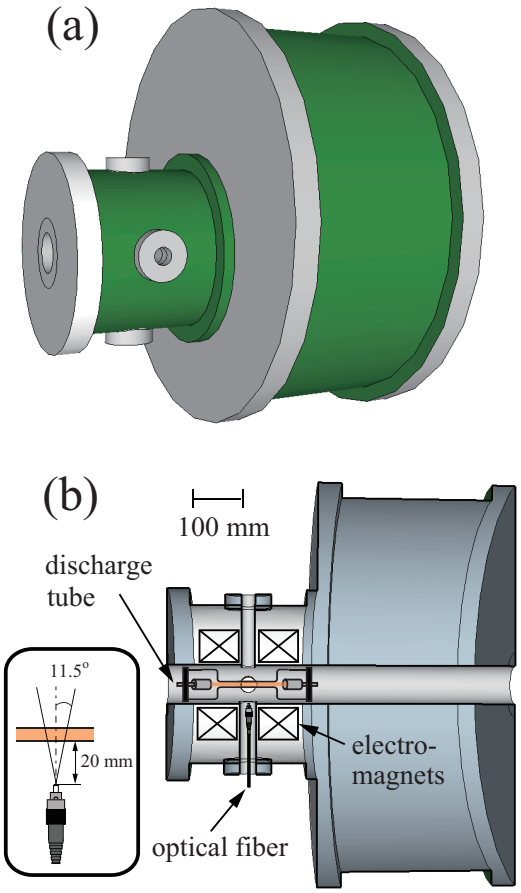

Figure 5: Schematic diagrams of the experimental apparatus: (a) appearance of the superconducting magnet and (b) horizontal cross-section on the axis of the magnet. The inset shows the acceptance angle of the optical fiber.

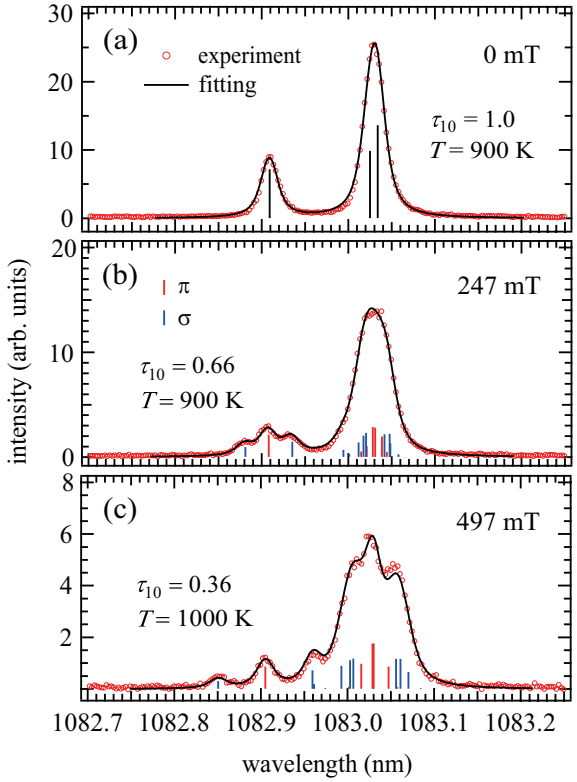

Figure 6: Measured and fitted spectral line shapes under magnetic field strengths of (a) 0, (b) 247, and (c) 497 mT.

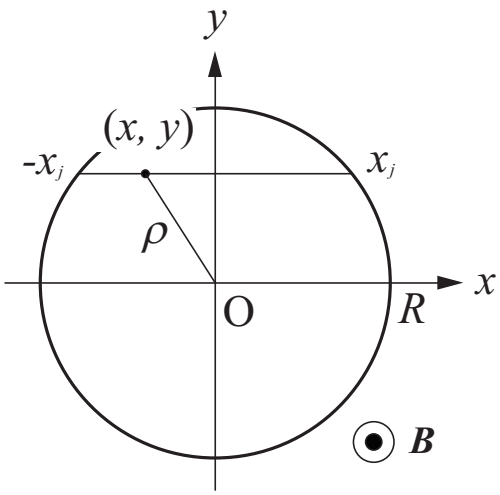

Figure 7: Schematic drawing of the coordinate system.

Table A1: Wavelengths of the transitions among the magnetic sublevels. 1082 should be added to all values. The indices denote $J'M'JM$, where J and M are the total angular momentum and magnetic quantum numbers in the weak field limit, respectively, and prime represents the upper state.

B (T)	λ - 1082 (nm)																		
	001-1	0010	0011	1-11-1	1-110	101-1	1010	1011	1110	1111	2-21-1	2-11-1	2-110	201-1	2010	2011	2110	2111	2211
0.0	0.9091	0.9091	0.9091	1.0250	1.0250	1.0250	1.0250	1.0250	1.0250	1.0250	1.0340	1.0340	1.0340	1.0340	1.0340	1.0340	1.0340	1.0340	1.0340
0.1	0.8980	0.9089	0.9199	1.0215	1.0325	1.0132	1.0242	1.0351	1.0160	1.0270	1.0395	1.0320	1.0430	1.0240	1.0350	1.0460	1.0265	1.0375	1.0285
0.2	0.8865	0.9084	0.9303	1.0169	1.0389	1.0004	1.0223	1.0442	1.0060	1.0279	1.0449	1.0311	1.0530	1.0155	1.0374	1.0593	1.0201	1.0421	1.0230
0.3	0.8747	0.9076	0.9404	1.0119	1.0448	0.9873	1.0201	1.0530	0.9955	1.0284	1.0504	1.0306	1.0635	1.0075	1.0404	1.0733	1.0142	1.0471	1.0175
0.4	0.8626	0.9064	0.9502	1.0067	1.0505	0.9741	1.0180	1.0618	0.9848	1.0286	1.0559	1.0304	1.0742	0.9999	1.0438	1.0876	1.0085	1.0523	1.0121
0.5	0.8501	0.9049	0.9597	1.0014	1.0562	0.9611	1.0159	1.0707	0.9740	1.0288	1.0614	1.0302	1.0850	0.9926	1.0473	1.1021	1.0028	1.0576	1.0066
0.6	0.8374	0.9031	0.9688	0.9960	1.0618	0.9482	1.0139	1.0797	0.9632	1.0289	1.0668	1.0301	1.0958	0.9854	1.0511	1.1168	0.9972	1.0630	1.0011
0.7	0.8243	0.9010	0.9777	0.9906	1.0673	0.9354	1.0121	1.0888	0.9523	1.0290	1.0723	1.0300	1.1067	0.9783	1.0550	1.1317	0.9917	1.0684	0.9956
0.8	0.8110	0.8986	0.9862	0.9852	1.0729	0.9228	1.0104	1.0981	0.9414	1.0290	1.0778	1.0300	1.1176	0.9714	1.0591	1.1467	0.9861	1.0738	0.9902
0.9	0.7974	0.8960	0.9946	0.9798	1.0784	0.9103	1.0089	1.1075	0.9305	1.0291	1.0833	1.0299	1.1285	0.9646	1.0632	1.1618	0.9806	1.0792	0.9847
1.0	0.7836	0.8931	1.0026	0.9744	1.0839	0.8980	1.0075	1.1171	0.9196	1.0291	1.0888	1.0299	1.1394	0.9579	1.0675	1.1771	0.9751	1.0846	0.9792
1.1	0.7695	0.8900	1.0105	0.9689	1.0894	0.8858	1.0063	1.1268	0.9087	1.0292	1.0942	1.0298	1.1504	0.9513	1.0718	1.1924	0.9696	1.0901	0.9737
1.2	0.7553	0.8867	1.0182	0.9635	1.0949	0.8737	1.0051	1.1366	0.8977	1.0292	1.0997	1.0298	1.1613	0.9448	1.0763	1.2078	0.9641	1.0955	0.9683
1.3	0.7409	0.8832	1.0256	0.9580	1.1004	0.8617	1.0041	1.1465	0.8868	1.0292	1.1052	1.0298	1.1722	0.9384	1.0808	1.2233	0.9586	1.1010	0.9628
1.4	0.7263	0.8796	1.0329	0.9526	1.1059	0.8498	1.0031	1.1565	0.8759	1.0292	1.1107	1.0298	1.1832	0.9320	1.0854	1.2388	0.9531	1.1065	0.9573
1.5	0.7115	0.8758	1.0401	0.9471	1.1114	0.8380	1.0023	1.1666	0.8650	1.0293	1.1162	1.0297	1.1941	0.9257	1.0900	1.2544	0.9476	1.1119	0.9518
1.6	0.6967	0.8719	1.0471	0.9416	1.1169	0.8263	1.0015	1.1768	0.8540	1.0293	1.1216	1.0297	1.2050	0.9195	1.0947	1.2701	0.9421	1.1174	0.9463
1.7	0.6816	0.8678	1.0540	0.9362	1.1224	0.8146	1.0008	1.1871	0.8431	1.0293	1.1271	1.0297	1.2160	0.9133	1.0995	1.2858	0.9366	1.1228	0.9409
1.8	0.6665	0.8636	1.0608	0.9307	1.1279	0.8031	1.0002	1.1974	0.8321	1.0293	1.1326	1.0297	1.2269	0.9071	1.1043	1.3016	0.9311	1.1283	0.9354
1.9	0.6513	0.8593	1.0675	0.9252	1.1334	0.7915	0.9996	1.2078	0.8212	1.0293	1.1381	1.0297	1.2379	0.9010	1.1092	1.3174	0.9256	1.1338	0.9299
2.0	0.6360	0.8550	1.0741	0.9198	1.1389	0.7801	0.9991	1.2183	0.8103	1.0293	1.1435	1.0297	1.2488	0.8949	1.1140	1.3332	0.9201	1.1392	0.9244
2.1	0.6206	0.8505	1.0806	0.9143	1.1444	0.7687	0.9987	1.2288	0.7993	1.0293	1.1490	1.0297	1.2598	0.8889	1.1190	1.3491	0.9147	1.1447	0.9190
2.2	0.6051	0.8460	1.0870	0.9088	1.1499	0.7573	0.9982	1.2393	0.7884	1.0293	1.1545	1.0297	1.2707	0.8829	1.1239	1.3650	0.9092	1.1502	0.9135
2.3	0.5896	0.8414	1.0933	0.9034	1.1553	0.7460	0.9978	1.2499	0.7774	1.0293	1.1600	1.0297	1.2817	0.8770	1.1289	1.3810	0.9037	1.1557	0.9080
2.4	0.5740	0.8367	1.0996	0.8979	1.1608	0.7346	0.9975	1.2605	0.7665	1.0293	1.1655	1.0297	1.2926	0.8710	1.1339	1.3970	0.8982	1.1611	0.9025
2.5	0.5583	0.8320	1.1059	0.8924	1.1663	0.7234	0.9972	1.2711	0.7555	1.0294	1.1709	1.0296	1.3036	0.8651	1.1390	1.4130	0.8927	1.1666	0.8971
2.6	0.5426	0.8272	1.1121	0.8870	1.1718	0.7121	0.9969	1.2818	0.7446	1.0294	1.1764	1.0296	1.3146	0.8592	1.1440	1.4290	0.8872	1.1721	0.8916
2.7	0.5268	0.8224	1.1182	0.8815	1.1773	0.7009	0.9966	1.2925	0.7337	1.0294	1.1819	1.0296	1.3255	0.8533	1.1491	1.4451	0.8818	1.1776	0.8861
2.8	0.5110	0.8176	1.1243	0.8760	1.1828	0.6897	0.9964	1.3032	0.7227	1.0294	1.1874	1.0296	1.3365	0.8475	1.1542	1.4611	0.8763	1.1830	0.8806
2.9	0.4952	0.8127	1.1303	0.8705	1.1882	0.6785	0.9961	1.3139	0.7118	1.0294	1.1929	1.0296	1.3474	0.8417	1.1594	1.4772	0.8708	1.1885	0.8752
3.0	0.4793	0.8077	1.1364	0.8651	1.1937	0.6674	0.9959	1.3247	0.7008	1.0294	1.1983	1.0296	1.3584	0.8359	1.1645	1.4933	0.8653	1.1940	0.8697

Table A2: Magnitudes of the square of the transition matrix element among the magnetic sublevels.

B (T)	$\mathfrak{S}$ ($\times 10^{20}$ m^2)																		
	001-1	0010	0011	1-11-1	1-110	101-1	1010	1011	1110	1111	2-21-1	2-11-1	2-110	201-1	2010	2011	2110	2111	2211
0.0	0.5984	0.5984	0.5984	0.8975	0.8975	0.8975	0.0000	0.8975	0.8975	0.8975	1.7951	0.8975	0.8975	0.2992	1.1967	0.2992	0.8975	0.8975	1.7951
0.1	0.5432	0.5958	0.6561	0.4296	1.3654	0.5807	0.1325	1.0819	0.4296	1.3654	1.7951	1.3654	0.4296	0.6712	1.0668	0.0570	1.3654	0.4296	1.7951
0.2	0.4910	0.5883	0.7158	0.2030	1.5921	0.3906	0.3285	1.0759	0.2030	1.5921	1.7951	1.5921	0.2030	0.9135	0.8782	0.0034	1.5921	0.2030	1.7951
0.3	0.4422	0.5762	0.7767	0.1097	1.6854	0.2989	0.4789	1.0172	0.1097	1.6854	1.7951	1.6854	0.1097	1.0539	0.7400	0.0011	1.6854	0.1097	1.7951
0.4	0.3970	0.5599	0.8382	0.0669	1.7282	0.2501	0.5950	0.9499	0.0669	1.7282	1.7951	1.7282	0.0669	1.1480	0.6401	0.0070	1.7282	0.0669	1.7951
0.5	0.3555	0.5402	0.8994	0.0446	1.7505	0.2207	0.6913	0.8830	0.0446	1.7505	1.7951	1.7505	0.0446	1.2189	0.5636	0.0126	1.7505	0.0446	1.7951
0.6	0.3178	0.5176	0.9597	0.0316	1.7634	0.2010	0.7755	0.8185	0.0316	1.7634	1.7951	1.7634	0.0316	1.2763	0.5019	0.0168	1.7634	0.0316	1.7951
0.7	0.2837	0.4931	1.0183	0.0236	1.7715	0.1867	0.8514	0.7570	0.0236	1.7715	1.7951	1.7715	0.0236	1.3247	0.4506	0.0197	1.7715	0.0236	1.7951
0.8	0.2530	0.4672	1.0748	0.0182	1.7768	0.1754	0.9209	0.6987	0.0182	1.7768	1.7951	1.7768	0.0182	1.3666	0.4070	0.0215	1.7768	0.0182	1.7951
0.9	0.2257	0.4407	1.1286	0.0145	1.7806	0.1660	0.9851	0.6439	0.0145	1.7806	1.7951	1.7806	0.0145	1.4033	0.3692	0.0225	1.7806	0.0145	1.7951
1.0	0.2014	0.4142	1.1795	0.0118	1.7833	0.1578	1.0446	0.5926	0.0118	1.7833	1.7951	1.7833	0.0118	1.4358	0.3363	0.0230	1.7833	0.0118	1.7951
1.1	0.1799	0.3880	1.2271	0.0098	1.7853	0.1504	1.0997	0.5449	0.0098	1.7853	1.7951	1.7853	0.0098	1.4648	0.3073	0.0230	1.7853	0.0098	1.7951
1.2	0.1609	0.3627	1.2715	0.0082	1.7868	0.1435	1.1507	0.5008	0.0082	1.7868	1.7951	1.7868	0.0082	1.4907	0.2816	0.0228	1.7868	0.0082	1.7951
1.3	0.1441	0.3384	1.3125	0.0070	1.7880	0.1370	1.1978	0.4602	0.0070	1.7880	1.7951	1.7880	0.0070	1.5139	0.2588	0.0223	1.7880	0.0070	1.7951
1.4	0.1294	0.3154	1.3503	0.0061	1.7890	0.1308	1.2412	0.4230	0.0061	1.7890	1.7951	1.7890	0.0061	1.5348	0.2385	0.0217	1.7890	0.0061	1.7951
1.5	0.1164	0.2937	1.3849	0.0053	1.7898	0.1250	1.2811	0.3890	0.0053	1.7898	1.7951	1.7898	0.0053	1.5537	0.2203	0.0211	1.7898	0.0053	1.7951
1.6	0.1049	0.2735	1.4167	0.0047	1.7904	0.1193	1.3177	0.3580	0.0047	1.7904	1.7951	1.7904	0.0047	1.5708	0.2039	0.0204	1.7904	0.0047	1.7951
1.7	0.0948	0.2546	1.4456	0.0041	1.7909	0.1139	1.3513	0.3298	0.0041	1.7909	1.7951	1.7909	0.0041	1.5863	0.1891	0.0196	1.7909	0.0041	1.7951
1.8	0.0859	0.2371	1.4720	0.0037	1.7914	0.1088	1.3821	0.3042	0.0037	1.7914	1.7951	1.7914	0.0037	1.6004	0.1758	0.0189	1.7914	0.0037	1.7951
1.9	0.0781	0.2210	1.4960	0.0033	1.7917	0.1038	1.4103	0.2809	0.0033	1.7917	1.7951	1.7917	0.0033	1.6132	0.1638	0.0181	1.7917	0.0033	1.7951
2.0	0.0711	0.2061	1.5179	0.0030	1.7921	0.0991	1.4361	0.2598	0.0030	1.7921	1.7951	1.7921	0.0030	1.6248	0.1529	0.0174	1.7921	0.0030	1.7951
2.1	0.0649	0.1924	1.5378	0.0027	1.7923	0.0947	1.4598	0.2406	0.0027	1.7923	1.7951	1.7923	0.0027	1.6355	0.1429	0.0167	1.7923	0.0027	1.7951
2.2	0.0594	0.1798	1.5559	0.0025	1.7926	0.0904	1.4814	0.2232	0.0025	1.7926	1.7951	1.7926	0.0025	1.6452	0.1339	0.0160	1.7926	0.0025	1.7951
2.3	0.0545	0.1681	1.5724	0.0023	1.7928	0.0863	1.5013	0.2074	0.0023	1.7928	1.7951	1.7928	0.0023	1.6542	0.1256	0.0153	1.7928	0.0023	1.7951
2.4	0.0502	0.1575	1.5874	0.0021	1.7930	0.0825	1.5196	0.1930	0.0021	1.7930	1.7951	1.7930	0.0021	1.6624	0.1180	0.0147	1.7930	0.0021	1.7951
2.5	0.0463	0.1476	1.6011	0.0019	1.7931	0.0788	1.5363	0.1799	0.0019	1.7931	1.7951	1.7931	0.0019	1.6699	0.1111	0.0140	1.7931	0.0019	1.7951
2.6	0.0428	0.1386	1.6137	0.0018	1.7933	0.0754	1.5517	0.1679	0.0018	1.7933	1.7951	1.7933	0.0018	1.6769	0.1047	0.0135	1.7933	0.0018	1.7951
2.7	0.0396	0.1303	1.6251	0.0016	1.7934	0.0721	1.5659	0.1570	0.0016	1.7934	1.7951	1.7934	0.0016	1.6833	0.0988	0.0129	1.7934	0.0016	1.7951
2.8	0.0368	0.1226	1.6357	0.0015	1.7935	0.0690	1.5790	0.1470	0.0015	1.7935	1.7951	1.7935	0.0015	1.6893	0.0934	0.0124	1.7935	0.0015	1.7951
2.9	0.0342	0.1155	1.6453	0.0014	1.7936	0.0661	1.5911	0.1379	0.0014	1.7936	1.7951	1.7936	0.0014	1.6948	0.0884	0.0119	1.7936	0.0014	1.7951
3.0	0.0319	0.1090	1.6542	0.0013	1.7937	0.0633	1.6022	0.1295	0.0013	1.7937	1.7951	1.7937	0.0013	1.6999	0.0838	0.0114	1.7937	0.0013	1.7951